Electronic Supplementary Material (ESI) for Nanoscale.

Electronic supplementary information

Electrochemical coating of different conductive polymers on diverse plasmonic metal nanocrystals

Wenzheng Lu, Tsz Him Chow, Yao Lu and Jianfang Wang*

Department of Physics, The Chinese University of Hong Kong, Shatin, Hong Kong SAR, China. E-mail: jfwang@phy.cuhk.edu.hk

Experimental

Growth of the plasmonic metal nanocrystals

The Au nanocrystals, including Au nanospheres, Au nanobipyramids, Au NRs and Au NPLs, were grown by seed-mediated methods in aqueous solutions according to previous reports.[1–4] The Pt and Pd nanocrystals were prepared in aqueous solutions using K_2PtCl_4 and K_2PdCl_4 as the precursors, respectively.[5,6]

Deposition of the plasmonic nanocrystals on ITO substrates

The plasmonic metal nanocrystals were drop-cast on ITO substrates. Typically, the as-grown nanocrystal solution (0.5 mL) was centrifuged and washed twice with deionized water. The precipitate was redispersed in deionized water (0.1 mL). The resultant solution was drop-cast on an ITO substrate and blown off with nitrogen gas after 1 min. To reduce the CTAB packing density on the Au NPLs, the surface CTAB molecules were removed by immersing the Au NPL-deposited ITO substrate in ethanol for 12 h. To realize a higher CTAB packing density on the Au NPLs, the Au NPL solution with a CTAB concentration at 0.1 M was drop-cast on an ITO substrate. For the preparation of the Au NR arrays, an ITO substrate was immersed in the Au NR solution in the presence of CTAB at a concentration of 5 μM and left undisturbed for 12 h, as reported previously.[7]

Electrochemical coating

The electrochemical coating was performed using an electrochemical workstation (CHI 760E). A typical three-electrode system was employed. An ITO substrate, a standard Ag/AgCl reference and a Pt wire were used as the working, reference and counter electrodes, respectively. All electrodes were immersed in the electrolyte solution. For PANI coating, the electrolyte solution was composed of HNO_3 (2 M) and aniline (0.1 M) in an aqueous solution. PANI was coated by cycling the potential from -0.20 to +0.80 V, +0.85 V and +0.90 V, respectively, at a rate of 25 mV s^{-1}, or by applying a constant potential at +0.80 V, +0.85 V or +0.90 V, respectively, for different periods of time. For PPy coating, $LiClO_4$ (0.1 M) and pyrrole (0.01 M) were used as the electrolyte. A potential cycling from -0.40 V to +0.60 V at a rate of 25 mV s^{-1} was performed. For PEDOT coating, $LiClO_4$ (0.1 M) and EDOT (0.01 M) were used as the electrolyte. A potential cycling from -0.10 V to +0.85 V at a rate of 25 mV s^{-1} was employed. For PI coating, a potential cycling from -0.10 V to +0.75 V at a rate of 25 mV s^{-1} was applied, and the electrolyte solution was made of $LiClO_4$ (0.1 M) and indole (0.01 M).

Electrochemical switching

The electrochemical switching was performed with the same experimental setup as the electrochemical coating, except for the electrolyte. The electrolyte solution was made from a monomer-free aqueous solution containing HNO_3 (0.5 M). To switch the PANI between the oxidized and reduced states, a constant electrochemical potential of -0.10 V (for the reduced state) or +0.50 V (for the oxidized state) was applied to the working electrode for 10 s.

H_2O_2 sensing

The H_2O_2 sensing was carried out by first electrochemically switching the PANI-coated Au NRs to the reduced state. The H_2O_2 solution at different concentrations from 1 µM to 100 mM was dropped on the nanostructures and maintained for 5 min. The optical measurements were carried out immediately after the ITO substrate was blown dried with nitrogen.

Characterization and optical measurements

SEM imaging was performed on a Schottky field-emission microscope (JEOL JSM-7800F) under a working voltage of 10 kV. Photographs were taken with a commercial digital camera (Nikon D7000). Extinction spectra were acquired on an ultraviolet/visible/near-infrared spectrophotometer (PerkinElmer Lambda 950). Single-particle dark-field scattering spectra were collected on a dark-field microscope (Olympus BX53M) integrated with a quartz-tungsten-halogen lamp (Philips, 100 W), a monochromator (Acton, SpectraPro 2360i) and a charge-coupled device (CCD) camera (Pixis 400). The CCD camera temperature was cooled to and kept at -70 °C during the measurements. A dark-field objective (100×, numerical aperture: 0.9) was employed for the excitation and the collection of the scattered light from the targeted nanostructures. The scattered light was directed to the CCD camera through an entrance slit of the monochromator. The scattering spectrum from the target nanostructure was corrected by subtracting the background spectrum taken from the adjacent region without any nanostructure and divided by the pre-calibrated optical response curve of the entire optical system.

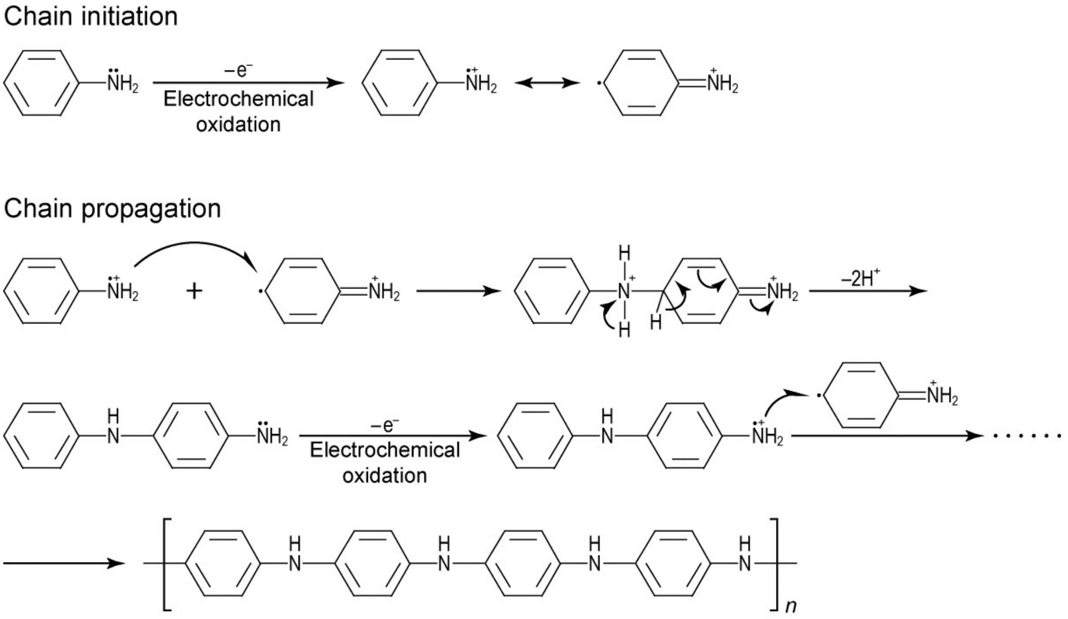

Fig. S1 Electrochemical polymerization of aniline.

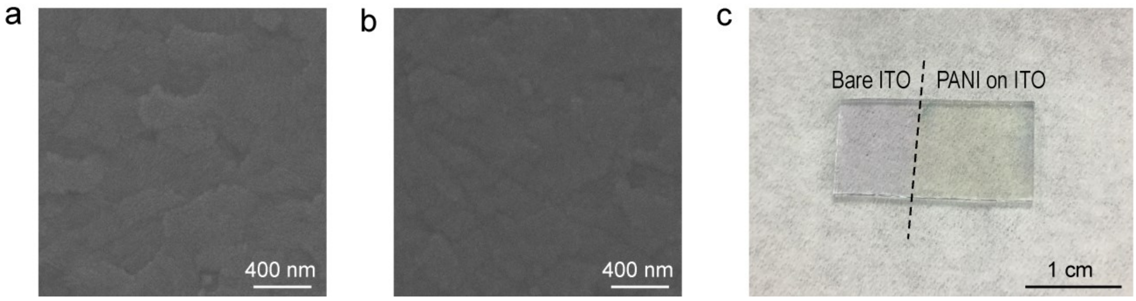

Fig. S2 Electrochemical coating of PANI on bare ITO substrates. (a) SEM image of an uncoated ITO substrate. (b) SEM image of an ITO substrate coated with a PANI film through electrochemical polymerization. (c) Photograph of the ITO substrate with a PANI film coated on the right side.

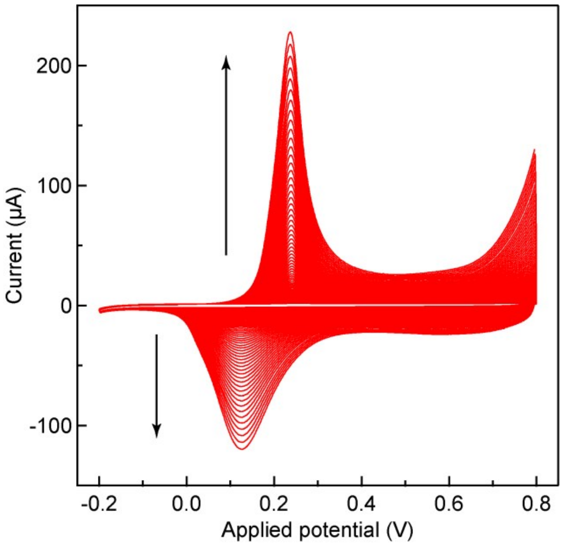

Fig. S3 Electrochemical *I*-*V* curves recorded under the VP condition. The electrochemical *I*-*V* curves were recorded on an electrochemical workstation using a cyclic voltammetry mode. The electrochemical coating was performed by varying the electrochemical potential from -0.20 V to +0.80 V (vs the Ag/AgCl reference) in 120 cycles with a voltage sweeping rate of 0.025 V s^{-1}. The top and bottom arrows indicate the increase of the current for the electrochemical oxidation and reduction of PANI, respectively, as the number of the coating cycles is increased. The oxidation and reduction peaks are located at +0.237 V and +0.125 V, respectively.

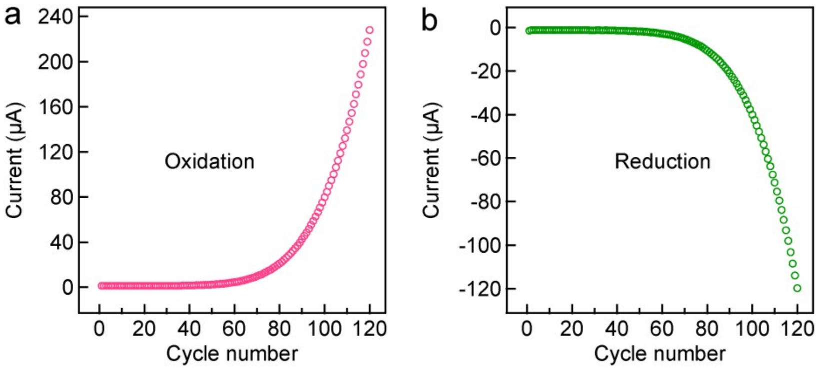

Fig. S4 Variation of the electrochemical current with the number of the coating cycles. (a) Currents at the oxidation peak of PANI in different coating cycles. (b) Currents at the reduction peak of PANI in different coating cycles. They were extracted from Figure S3.

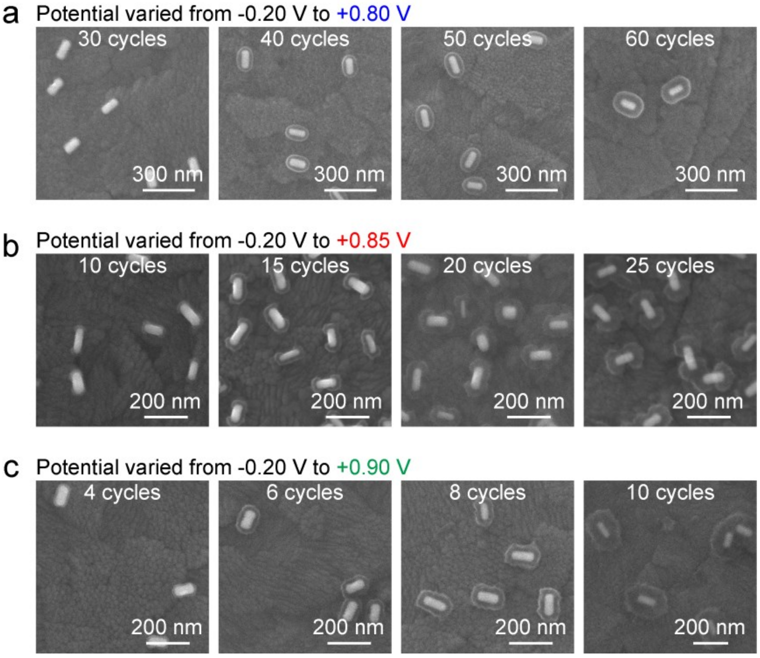

Fig. S5 Electrochemical coating under the VP condition. (a) SEM images of the PANI-coated Au NRs prepared in the potential range of -0.20 V to +0.80 V for 30, 40, 50 and 60 coating cycles, respectively. (b) SEM images of the PANI-coated Au NRs prepared in the potential range of -0.20 V to +0.85 V for 10, 15, 20 and 25 coating cycles, respectively. (c) SEM images of the PANI-coated Au NRs prepared in the potential range of -0.20 V to +0.90 V for 4, 6, 8 and 10 coating cycles, respectively.

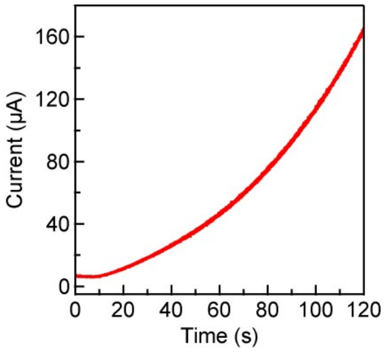

Fig. S6 Electrochemical *I-t* curve recorded under the CP condition. The constant electrochemical potential of +0.85 V was applied with a coating time of 120 s.

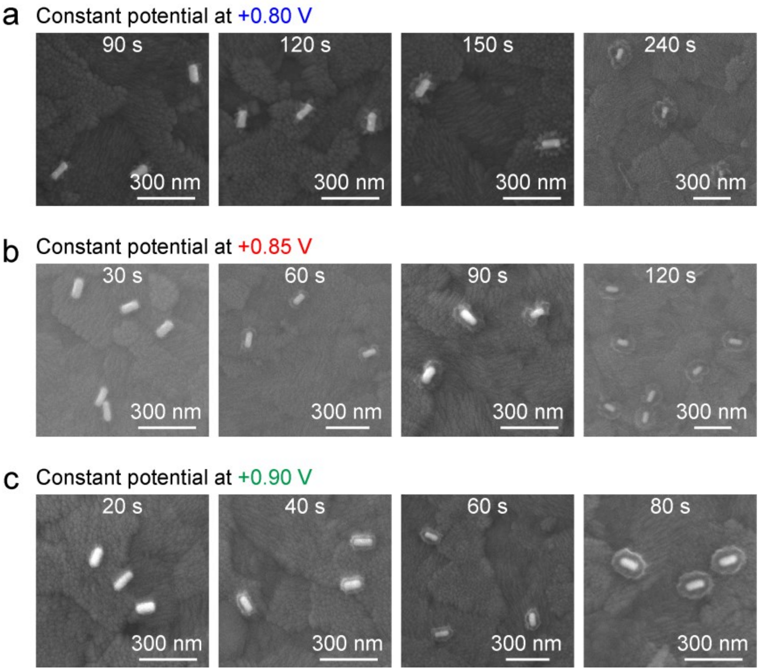

Fig. S7 Electrochemical coating under the CP condition. (a) SEM images of the PANI-coated Au NRs obtained at the constant potential of +0.80 V for 90 s, 120 s, 150 s and 240 s, respectively. (b) SEM images of the PANI-coated Au NRs obtained at the constant potential of +0.85 V for 30 s, 60 s, 90 s and 120 s, respectively. (c) SEM images of the PANI-coated Au NRs obtained at the constant potential of +0.90 V for 20 s, 40 s, 60 s and 80 s, respectively.

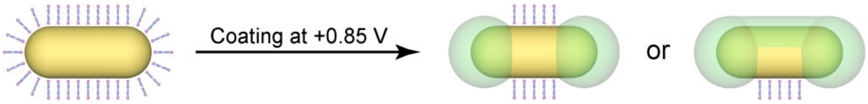

Fig. S8 Schematics illustrating the formation of the two-end coating and dent coating on Au NRs. CTAB molecules adsorbed on the Au NR pack less compactly at the ends of the NR than on the side facets because of the difference in the geometrical curvature. This causes a stronger obstruction on the side facets, leaving the ends for the preferential adsorption of the monomers. As a result, the two-end coating occurs under a moderate coating condition (+0.85 V). The dent coating is produced similarly except that the CTAB molecules packed on one side of the Au NR is destroyed during the deposition of the Au NRs on the substrate.

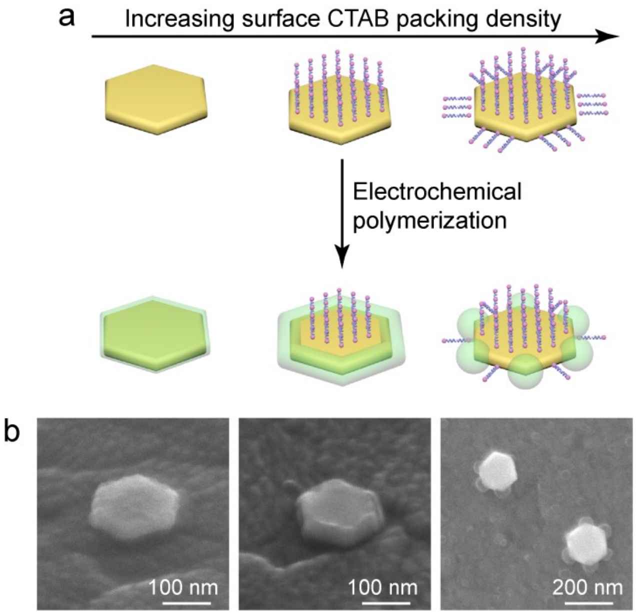

Fig. S9 Site-selective coating of PANI on the Au NPLs. (a) Schematics illustrating the polymer coating on the Au NPLs with increasing CTAB surface packing densities. The electrochemical polymerization was performed under the VP condition in the potential range from -0.20 V to +0.85 V for 10 coating cycles. (b) 45°-tilted-view SEM image of a Au NPL with PANI coated uniformly (left), 45°-tilted-view SEM image of a Au NPL with PANI coated at the side edges (middle), and SEM image of the Au NPLs with PANI coated at the corners.

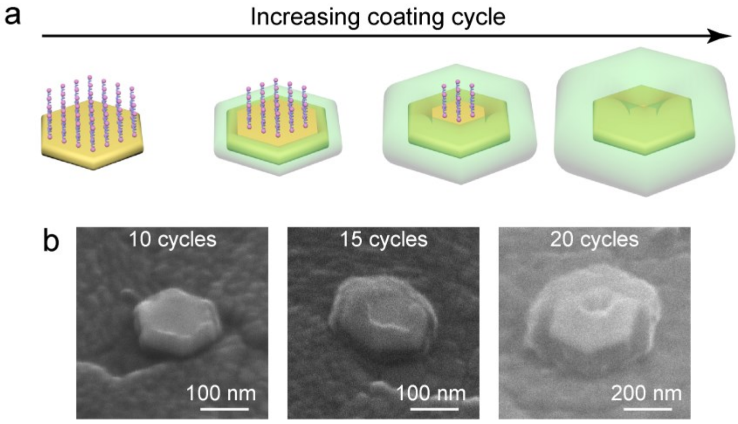

Fig. S10 Au NPLs with PANI coated at the edges. (a) Schematics illustrating the changes in the coating of PANI on the side edges of the Au NPLs with increasing coating cycles. (b) Tilted-view SEM images of the PANI-coated Au NPLs prepared in 10, 15 and 20 coating cycles, respectively. The coating was performed under the VP condition in the potential range from -0.20 V to +0.85 V. The samples were tilted by 45°.

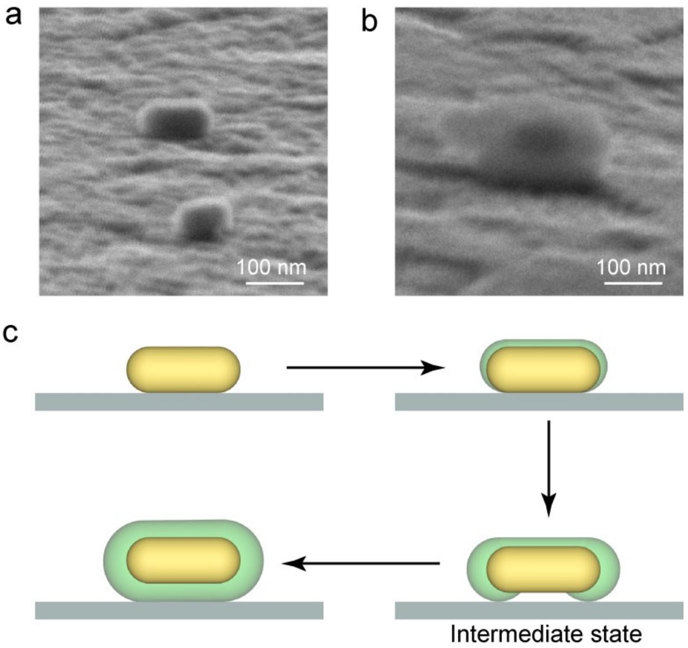

Fig. S11 Electrochemical coating underneath the Au NRs. (a) Tilted-view SEM image of the Au NRs with a coated PANI layer that grows on the nanocrystal surface with a moderate coating thickness. (b) Tilted-view SEM image of a Au NR with a thick coated PANI layer. The SEM images reveal that the polymer can grow underneath the Au NRs if the coated polymer layer is thick enough. The samples were tilted by 75° during SEM imaging. (c) Schematics illustrating a possible mechanism for the polymer coating process on the Au NR. The Au NR can be slightly levitated over the substrate because of the polymer coating at the ends of the Au NR, as shown in the intermediate state.

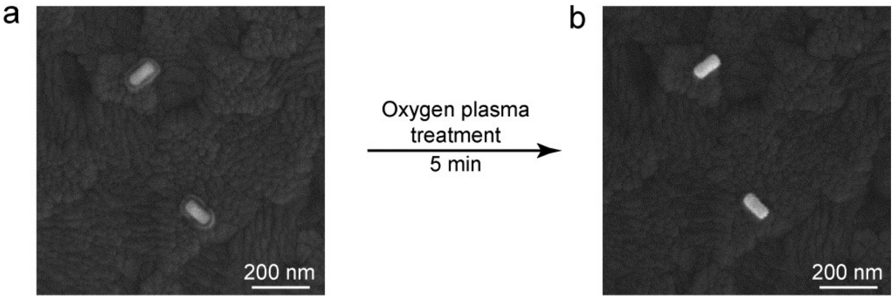

Fig. S12 Removal of the coated polymer. (a) SEM image of the PANI-coated Au NRs. (b) SEM image of the same Au NRs after the oxygen plasma treatment. The oxygen plasma treatment can easily remove the coated polymer from metal nanocrystals. With the plasma treatment, the electrochemical coating can be repeated many times on the same metal nanocrystals.

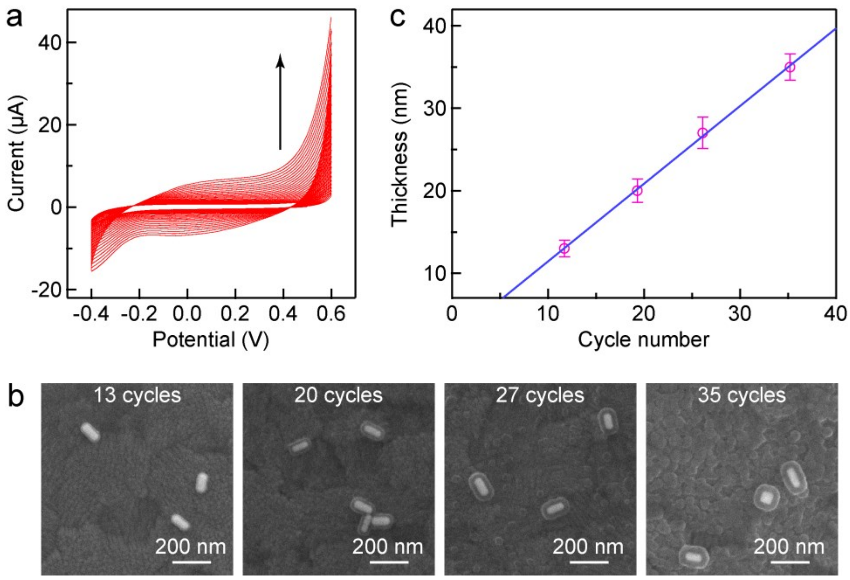

Fig. S13 Electrochemical coating of PPy. (a) *I*-*V* curves recorded during the electrochemical coating of PPy under the VP condition. The arrow indicates the increasing current with the number of the coating cycles. (b) SEM images of the PPy-coated Au NRs obtained in different coating cycles. (c) Thickness evolution with the number of the coating cycles.

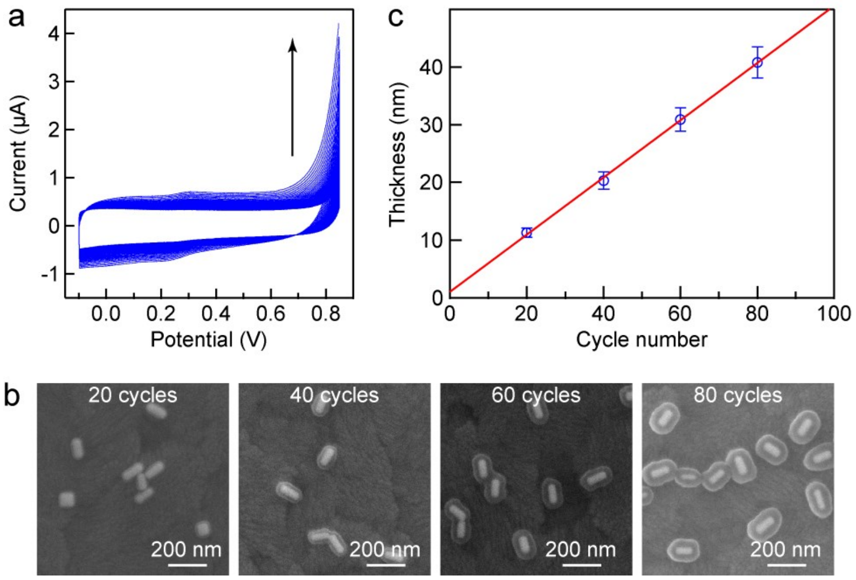

Fig. S14 Electrochemical coating of PEDOT. (a) *I*-*V* curves recorded during the electrochemical coating of PEDOT under the VP condition. The arrow indicates the increasing current with the number of the coating cycles. (b) SEM images of the PEDOT-coated Au NRs obtained in different coating cycles. (c) Thickness evolution with the number of the coating cycles.

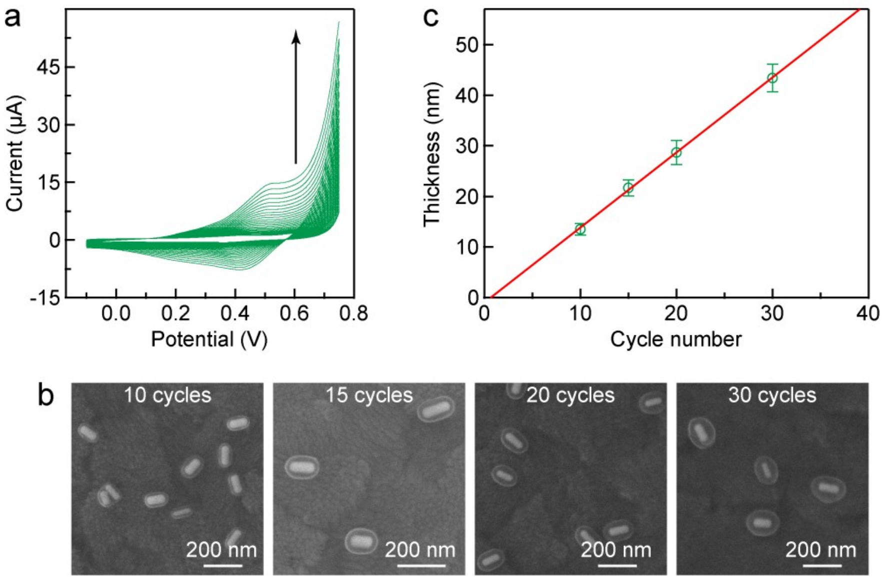

Fig. S15 Electrochemical coating of PI. (a) *I*-*V* curves recorded during the electrochemical coating of PI under the VP condition. The arrow indicates the increasing current with the number of the coating cycles. (b) SEM images of the PI-coated Au NRs obtained in different coating cycles. (c) Thickness evolution with the number of the coating cycles.

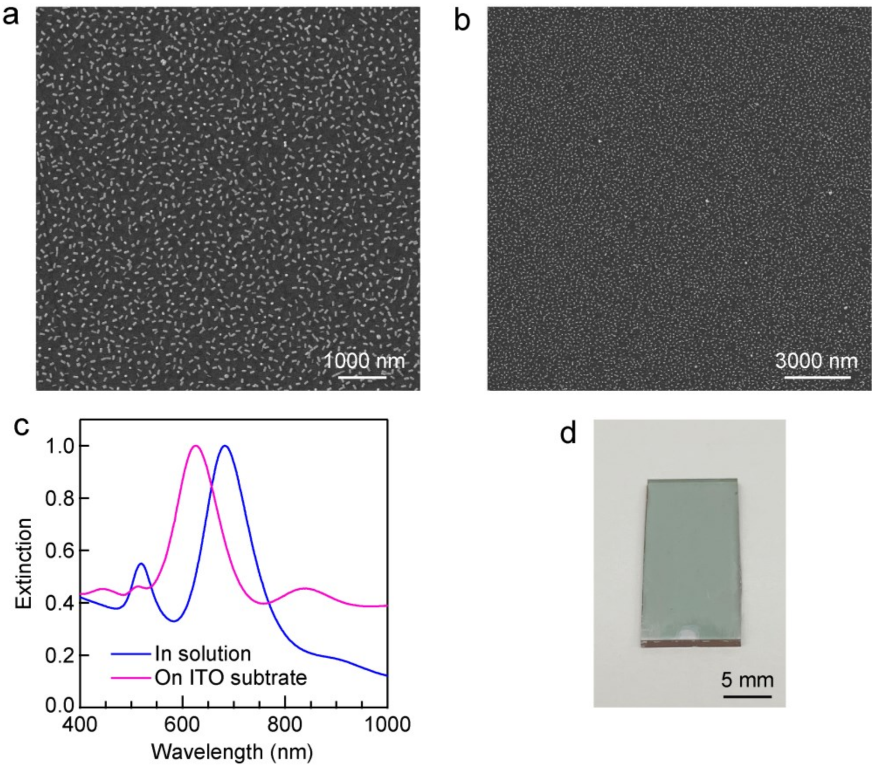

Fig. S16 Au NR arrays. (a) SEM image of the Au NR array on an ITO substrate at high magnification. (b) SEM image of the same Au NR array at low magnification. The Au NRs are uniformly distributed on the ITO substrate without clear aggregation. (c) Normalized extinction spectra of the Au NRs in an aqueous solution and deposited on the ITO substrate. The plasmon peaks are blueshifted after the deposition due to the change of the surrounding dielectric environment. The small bump at 830 nm for the Au NR array is ascribed to the presence of weak plasmon coupling. (d) Photograph of an ITO substrate deposited with a macroscale Au NR array.

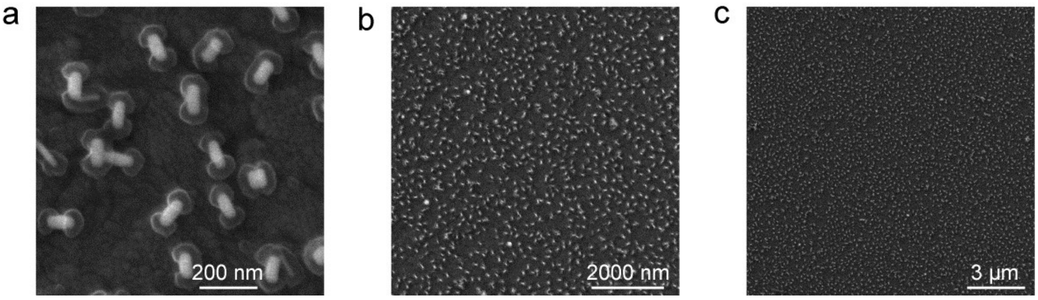

Fig. S17 PANI-coated Au NR arrays. (a–c) SEM images of a PANI-coated Au NR array with the two-end and dent coating morphologies at high, medium and low magnifications, respectively.

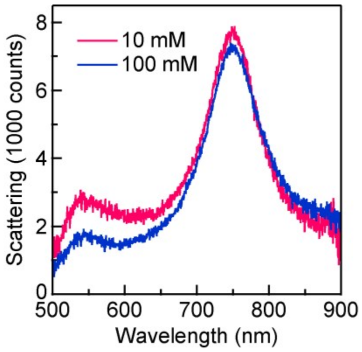

Fig. S18 Single-particle scattering spectra. The spectra were acquired on a single PANI-coated Au NR treated with H_2O_2 solutions at 10 mM and 100 mM, respectively.

References

1 F. Qin, T. Zhao, R. B. Jiang, N. N. Jiang, Q. F. Ruan, J. F. Wang, L.-D. Sun, C.-H. Yan and H.-Q. Lin, *Adv. Opt. Mater.*, 2016, **4**, 76–85.

2 Q. F. Ruan, L. Shao, Y. W. Shu, J. F. Wang and H. K. Wu, *Adv. Opt. Mater.*, 2014, **2**, 65–73.

3 Q. Li, X. L. Zhuo, S. Li, Q. F. Ruan, Q.-H. Xu and J. F. Wang, *Adv. Opt. Mater.*, 2015, **3**, 801–812.

4 H. J. Chen, L. Shao, Q. Li and J. F. Wang, *Chem. Soc. Rev.*, 2013, **42**, 2679–2724.

5 B. C. Yang, C. M. Zhao, M. D. Xiao, F. Wang, C. H. Li, J. F. Wang and J. C. Yu, *Small*, 2013, **9**, 1003–1007.

6 F. Wang, C. H. Li, L.-D. Sun, C.-H. Xu, J. F. Wang, J. C. Yu and C.-H. Yan, *Angew. Chem., Int. Ed.*, 2012, **51**, 4872–4876.

7 L. Shao, Q. F. Ruan, R. B. Jiang and J. F. Wang, *Small*, 2014, **10**, 802–811.